MATERIALS SCIENCE

Ultrasensitive and ultrathin phototransistors and photonic synapses using perovskite quantum dots grown from graphene lattice

Basudev Pradhan[1]*†, Sonali Das[1†], Jinxin Li[2], Farzana Chowdhury[1], Jayesh Cherusseri[1], Deepak Pandey[3], Durjoy Dev[1,4], Adithi Krishnaprasad[1,4], Elizabeth Barrios[1,3], Andrew Towers[1,5], Andre Gesquiere[1,2,5], Laurene Tetard[1,3,4], Tania Roy[1,3‡], Jayan Thomas[1,2,3‡]

Organic-inorganic halide perovskite quantum dots (PQDs) constitute an attractive class of materials for many optoelectronic applications. However, their charge transport properties are inferior to materials like graphene. On the other hand, the charge generation efficiency of graphene is too low to be used in many optoelectronic applications. Here, we demonstrate the development of ultrathin phototransistors and photonic synapses using a graphene-PQD (G-PQD) superstructure prepared by growing PQDs directly from a graphene lattice. We show that the G-PQDs superstructure synchronizes efficient charge generation and transport on a single platform. G-PQD phototransistors exhibit excellent responsivity of 1.4×10^8 AW^{-1} and specific detectivity of 4.72×10^{15} Jones at 430 nm. Moreover, the light-assisted memory effect of these superstructures enables photonic synaptic behavior, where neuromorphic computing is demonstrated by facial recognition with the assistance of machine learning. We anticipate that the G-PQD superstructures will bolster new directions in the development of highly efficient optoelectronic devices.

INTRODUCTION

Graphene emerged as the dream material for electronic and optoelectronic applications due to its broad spectral bandwidth, excellent carrier transport properties with very high mobility (electron mobility, >15,000 cm^2·V^{-1}·s^{-1}), and exceptional stability in ambient conditions and outstanding flexibility (*1*, *2*). A plethora of composites and devices have been developed for applications in energy harvesting and storage, photodetectors, and transistors (*3*). However, a single layer of graphene absorbs only 2.3% of incident visible light (*4*). Moreover, to date, the responsivity of graphene photodetectors has been limited to about 10^{-2} A W^{-1}. These limitations critically impede the use of graphene in optoelectronic and photonic devices (*4*). On the other hand, organic-inorganic halide perovskite quantum dots (PQDs) have risen as attractive materials for optoelectronic devices due to their bandgap tunability across the visible spectrum, high photoluminescence (PL) quantum yield, narrow emission spectrum, and high extinction coefficients (*5*). A major drawback is their inferior charge transport compared with graphene.

To improve the performance of graphene-based phototransistors, various approaches such as PQDs in the form of bilayers (*6*) or heterostructures (*7*) have been pursued. A phototransistor composed of a two-dimensional (2D) perovskite thin film deposited on graphene by spin coating exhibited responsivity ~10^5 A W^{-1} at 530 nm (*7*). Pan *et al.* (*6*) has also demonstrated photoresponsivity of 1.15×10^5 A W^{-1} at 520 nm using spin-coated formamidinium lead halide PQDs on a graphene layer. Presently, most of the PQD films prepared as the active layer of phototransistors by various deposition techniques have a minimum thickness of at least 100 nm. The highest photoresponsivity reported for a graphene-based phototransistor is 10^7 A W^{-1}, measured with an infrared phototransistor prepared by spin coating lead sulfide (PbS) quantum dots (QDs) on chemical vapor deposition–grown graphene (*8*). Growing PQDs from a graphene lattice to enhance charge transfers between the two moieties constitutes an entirely new direction for electronic and optoelectronic device applications.

Here, we demonstrate that the strong photogeneration efficiency of methylammonium lead bromide PQDs can be exploited by growing PQDs from the lattice of a single-layer graphene by a defect-mediated process. The rationale for designing this hybrid superstructure stems from the ability of PQDs to absorb light and generate charge carriers. The charges generated are transferred to graphene, which transports the carriers across the active layer of the device. Through the implementation of this thin superstructure in a phototransistor geometry, we produce a photoresponsivity of 1.4×10^8 A W^{-1} at 430 nm and a specific detectivity (D*) of 4.72×10^{15} Jones, which is, by far, the best responsivity and detectivity across similar devices reported to date. This is promising for the development of highly efficient optoelectronic materials for high-speed communications, sensing, ultrasensitive cameras, and high-resolution imaging and displays (*9*). In addition, we find the graphene-PQD (G-PQD) superstructure to behave as a photonic synapse with low energy consumption of 36.75 pJ per spike that mimics crucial characteristics of its biological equivalent, with unique optical potentiation and electrical habituation function. This is critical for pattern recognition. This enables the building of a hardware unit for the neuromorphic architecture to mimic the human brain functionalities, which is critical for applications such as pattern recognition.

[1]NanoScience Technology Center, University of Central Florida, Orlando, FL 32826, USA. [2]CREOL, The College of Optics and Photonics, University of Central Florida, Orlando, FL 32816, USA. [3]Department of Materials Science and Engineering, University of Central Florida, Orlando, FL 32816, USA. [4]Department of Physics, University of Central Florida, Orlando, FL 32816, USA. [5]Department of Chemistry, University of Central Florida, Orlando, FL 32816, USA.
*Present address: Centre of Excellence in Green and Efficient Energy Technology, Department of Energy Engineering, Central University of Jharkhand, Brambe, Ranchi, Jharkhand 835205, India.
†These authors contributed equally to this work.
‡Corresponding author. Email: jayan.thomas@ucf.edu (J.T.); tania.roy@ucf.edu (T.R.)

RESULTS

Growing PQDs from graphene lattice

Among the techniques used to produce PQDs with very high PL quantum yield (*10*), ligand-assisted reprecipitation (LARP) stands out as a very versatile approach. LARP uses the mixing of polar and nonpolar solvents to synthesize PQDs at room temperature. This strategy is sufficiently mature to control the size and morphology of the PQDs (*11*). PQDs with a diameter below 4 nm have previously been grown, exhibiting enhanced quantum confinement (*12*). Following similar considerations, we initiate the growth of PQDs directly on the active sites of graphene monolayer surfaces to form the superstructure. An antisolvent toluene was added onto a graphene layer previously wetted with perovskite precursor to initiate the seeding, which was followed by crystal growth, as illustrated in Fig. 1A. We explain the growth of PQDs on the graphene layer by a two-step growth model. First, when a large volume of the antisolvent toluene was injected onto the precursor-coated graphene, a highly disordered spherical perovskite droplet with high concentration and large density fluctuations was formed on the graphene surface as well as in the toluene solution due to the excess of precursors (*13*). Next, perovskite embryos formed on the graphene sheet as well as in the toluene solution, under saturation conditions, which transformed into a stable perovskite nucleus inside the droplet beyond the critical size required for crystal formation (*14*). With their high Gibbs surface free energy, we find that the defects in the graphene layer provide preferential sites for the embryo formation, thereby nucleating the PQDs. It is also possible that collisions between the disordered droplet and the graphene layer led to contact nucleation (fig. S1). Electrostatic attraction with the graphene layer may also contribute to the growth via strong immobilization of the clusters formed. We find the proximity to the critical point of nucleation to decrease the Gibbs surface free energy barrier for crystallization and consequently increase the rate of nucleation. The PQDs once grown from the graphene sample were washed continuously with a nonsolvent for about 10 min to remove any PQDs, which were not grown from, but just adsorbed, on the graphene surface.

We analyze the synthesized G-PQD hybrid material by transmission electron microscopy (TEM), as shown in Fig. 1 (B to E). Figure 1B indicates that the grown PQDs were randomly distributed on the graphene layers, with a denser population along the graphene edges. We surmise that defect sites or dangling bonds on the edges favor nucleation sites for the PQDs. We find that the PQDs grown on graphene by heterogeneous nucleation have an average diameter of 3.1 nm with a size deviation of 0.5 nm (Fig. 1, B and C) for a 30-min growth process. Figure 1C reveals the spherical shape of the PQDs over the graphene surface, while Fig. 1D indicates the interplanar (*d*) spacing of 0.27 nm, which corresponds to the (201) lattice plane in PQDs. Fast Fourier transform (FFT) analysis (Fig. 1D, inset) confirms that the zone axis of these QDs is along the (201) direction, which is consistent with the x-ray diffraction (XRD) results (Fig. 1F). The growth of PQDs on the graphene layer is further confirmed by the TEM image in Fig. 1E, where we observe lattice distortions. We attribute these to the stress developed in the graphene lattice upon PQD crystal growth. As seen in the inset, the spectra of pristine PQDs and G-PQDs both exhibit similar major peaks at 3.3°, 4.4°, 6.5°, 9.0°, and 15.4°, corresponding to (011), (101), (201), (141), and (100) crystal planes, respectively. This confirms the crystallinity of the structures formed in G-PQDs (*15*). We attribute the low peak intensities observed in the case of G-PQDs to the low density of PQDs on the single-layer graphene compared with the density of the pure PQD solution drop casted for the measurements.

The binding energies in the pristine PQDs and G-PQDs were evaluated using x-ray photoelectron spectroscopy (XPS). In pristine PQDs (fig. S2), the XPS spectra mostly coincided with the signature peaks of the bulk methylammonium lead bromide perovskite (*5*), especially for Pd-4f and Br-3d energy states. Binding energies at 67.58 and 68.62 eV correspond to inner and surface ions, respectively (*5*). The ratio of intensity of the two bands suggests that Br bonds were more prevalent in the core of the QDs than at their surface. The N-1s binding energies confirm the existence of two chemical environments of the N element with bands at 398.21 and 400.86 eV, corresponding to N-C and amine ($-NH_2$) ions, respectively. The Pb-4f spectrum also exhibited two peaks positioned at 137.77 and 142.63 eV, corresponding to the levels of Pb-$4f_{7/2}$ and Pb-$4f_{5/2}$ associated with Pb^{2+} in $PbBr_3^-$ (*16*), respectively. The C-1s spectrum with peaks at 284.03 and 284.43 eV confirms the presence of C—H/C—C and C—N bonds, respectively. All core-level XPS spectra corresponding to Pb-4f, Br-3d, C-1s, and N-1s (fig. S3) exhibited an increase in binding energies in G-PQDs compared with PQDs. The C-1s spectrum of G-PQDs also revealed sp^2 bonding with the apparition of a peak at 284.09 eV. We note that these results indicate binding between PQDs and the graphene layers, as evident from the fact that nonbound bilayer systems consisting of $CsPbBr_3$ QD/graphene oxide composite (*17*) and organic molecule-graphene interfaces previously characterized with XPS showed no signs of change in binding energies.

We further investigate the effect of growing PQDs on the graphene sheet with Raman spectroscopy. Pristine graphene exhibited the signature of a high-quality single layer, with a band ~1580 cm^{-1} corresponding to the stretching of the C—C bond in the plane (Fig. 1G), which is in agreement with the change in binding energies observed with XPS. To test the attachment of PQDs on a graphene surface, we drop casted a film of preprepared PQDs on graphene. The Raman spectra of graphene were not affected in this case (Fig. 1G). However, we find that in G-PQDs, the shift of a G band to a lower wavelength accompanied the apparition of a D band at ~1340 cm^{-1}. We attribute the D band in graphene to a zone boundary mode (A_{1g}) usually found at an armchair edge of graphene sheets. The results, thus, suggest that the growth of the PQDs created a sufficiently large density of local armchair edges in the graphene sheets to be detected by Raman spectroscopy.

Optical absorption is an important parameter for a highly sensitive photodetector. The grown G-PQD film absorbs in the visible wavelength region with a maximum of 434 nm and a secondary band maximum of 451 nm (Fig. 2A). We attribute these to two different sizes of PQDs grown on the graphene layer. The 434-nm band corresponded to the smaller PQDs. The PL spectrum exhibited peaks at 462 and 479 nm corresponding to a bandgap of 2.6 to 2.7 eV. The steady-state PL intensity decreased in G-PQD superstructures compared with pristine PQD film, which we attribute to additional charge transfer pathways provided by graphene in addition to the intrinsic radiative channels for excited-state charge transfer (*17*). Together, these results suggest that the G-PQD layer is a potential candidate for high-performing phototransistors detecting at blue illumination.

To further understand the photophysical properties of the material, the excited-state dynamics of the G-PQD superstructure were probed with time-correlated single photon counting (TCSPC). While the PQDs on a glass substrate exhibited a biexponential decay similar to

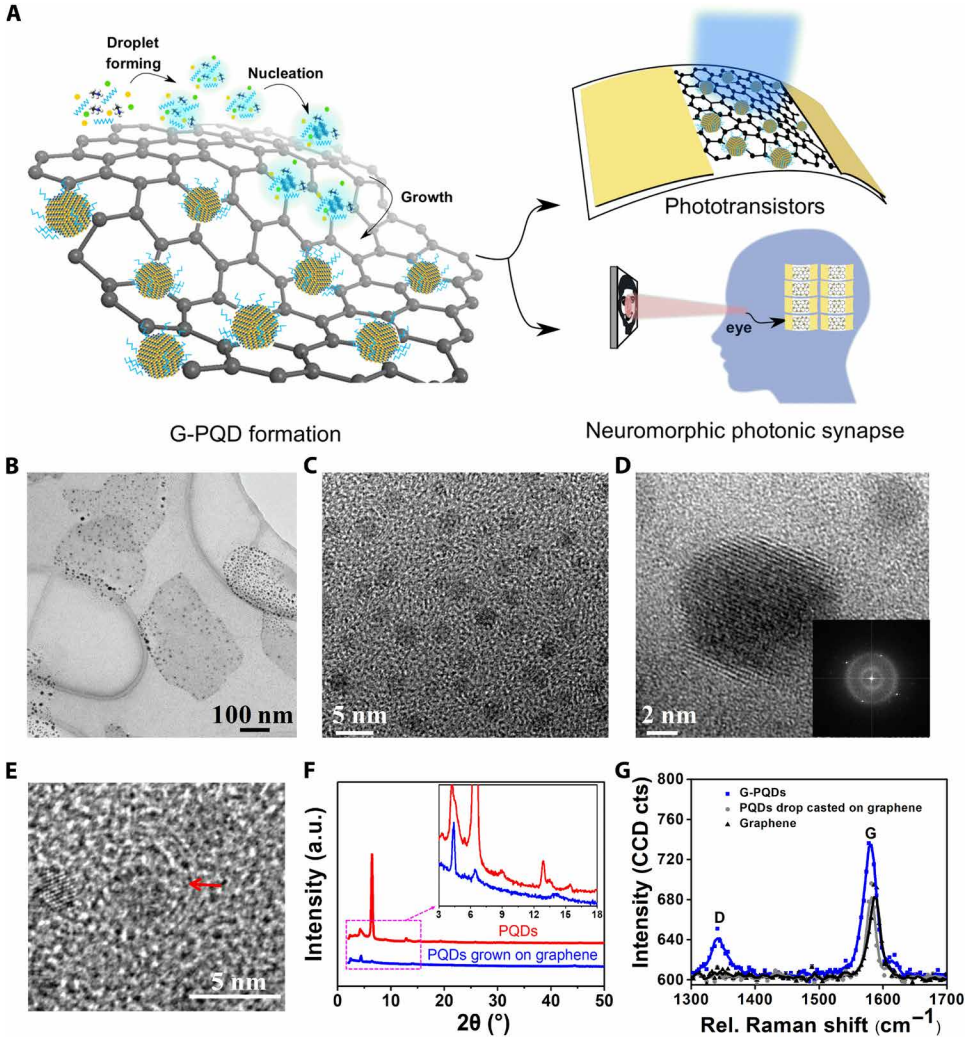

Fig. 1. G-PQD superstructure. (**A**) Schematic showing the growth of PQDs on graphene to form the G-PQD superstructure and the proposed applications. (**B**) TEM image of PQDs grown on a single layer of graphene sheets. (**C**) TEM image of the PQDs distributed on the G-PQD superstructure. (**D**) High-resolution TEM (HRTEM) image of the PQDs grown on graphene. Inset shows the corresponding FFT image. (**E**) HRTEM image of stress-induced changes in the graphene lattice due to the growth of PQDs (red arrow indicates distortion). (**F**) XRD spectra of pristine PQDs (red) and G-PQDs (blue) grown on silicon [inset: enlarged region; units remain the same, 3.3°, 4.4°, 6.5°, 9.0°, and 15.4° corresponding to (011), (101), (201), (141), and (100) crystal planes, respectively]. a.u., arbitrary units. (**G**) Raman spectra of pristine graphene (black), PQDs drop casted on graphene (gray), and PQDs grown on graphene (blue). CCD, charge-coupled device.

previously reported literature (*18*) with an average fluorescence decay time of 2747 ns, G-PQDs exhibited an average fluorescence decay time of 749 ns (Fig. 2B). Single-layer graphene has displayed similar quenching effects with previously reported perovskite nanoparticles and PQDs on single-layer graphene deposited by spin-coating methods (*19*). We believe that the longer fluorescence lifetimes observed in this study along with reported low exciton binding energy of perovskite materials could infer a photoinduced electron transfer mechanism as the predominant pathway for the quenching effects. Overall, the observed PL quenching indicates fast charge transfer in G-PQD superstructure due to high carrier mobility in graphene and the direct contact between the two components.

The growth of PQDs on graphene may facilitate charge transfer through π-π electron interactions between PQDs and the sp^2-hybridized graphene layer. Previously reported density functional theory (DFT) studies confer some insights into the electronic properties of the

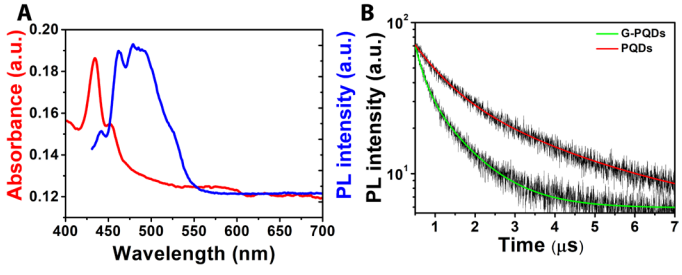

Fig. 2. UV-vis and PL spectra. (**A**) Ultraviolet-visible (UV-vis) absorption (red) and PL spectra (blue) of the G-PQD superstructure film. (**B**) PL decay profiles of PQD (red) and G-PQD films (green).

two different termination planes in perovskite crystals (*20*). It is important to understand the surface termination of perovskite crystals because heterogeneous nucleation of PQDs likely initiates

at defect sites (*21*) of graphene. According to DFT calculations, two possible terminations may occur during perovskite crystal formation of $CH_3NH_3PbI_3$ (*20*): (i) MAI termination (MA ion and I atoms in the plane) or (ii) PbI_2 termination (Pb and I atoms in the plane). It is demonstrated that Pb atoms in the PbI_2 termination plane and I atoms in the MAI termination plane comprise unhybridized p orbitals. Similar to $CH_3NH_3PbI_3$, there can be two possible terminations in the CH_3NH_3Br PQDs (*22*): (i) CH_3NH_3Br termination (MA ion and Br atoms in the termination plane) or (ii) $PbBr_2$ termination (Pb and Br atoms in the termination plane), as shown in fig. S4. Therefore, the Pb-6p orbitals and Br-4p orbitals on the terminated planes of PQDs can overlap with the unhybridized 2p orbitals of the carbon atoms of graphene. As the efficacy of charge transfers at the interface of PQD and graphene depends on the overlap of the π orbitals, the grown PQDs can transfer charges more efficiently than other heterostructures prepared by deposition techniques such as spin coating. However, the methyl ammonium ion ($CH_3NH_3^+$) does not directly take part in the charge transfer because it is caged in the corner sharing eight PbI_6^{-4} octahedra and is only hydrogen bonded to iodine atoms.

Highly sensitive ultrathin phototransistors

The aforementioned characterizations imply a direct growth of PQDs on the graphene surface, which facilitates an efficient charge transfer from PQDs to graphene. The charge generation and transfer efficiency of this superstructure were evaluated in a phototransistor geometry fabricated on a silicon dioxide/silicon wafer (fig. S5A). In this configuration, graphene constitutes a carrier transport channel, and PQDs play the role of the photoabsorbing material, as shown in Fig. 3A (inset). The pristine graphene used for this experiment was hole dominated. The current-voltage (drain current I_{DS} versus drain voltage V_{DS}) characteristics of the phototransistor in dark conditions and under 440-nm illumination with zero gate voltage are shown in Fig. 3A. These I_{DS}-V_{DS} curves indicate an ohmic behavior both for the forward and reverse bias, without any trace of hysteresis. We observe a substantial enhancement in photocurrent with an increase in illumination intensity. The phototransistor responsivity (R) was calculated as the ratio of the photocurrent density J_{ph} to incident light intensity L_{light}

$$R = J_{ph}/L_{light} \quad (1)$$

Figure 3B represents R over the 300- to 700-nm range. The photoresponsivity reaches a maximum at 430 nm, which matches with G-PQD absorbance peak, but slowly decreases in the 430- to 700-nm range. The G-PQD superstructure phototransistor shows a photoresponsivity of 1.4×10^8 A W^{-1}, which is among the highest reported responsivity, to the best of our knowledge. A very tight distribution of the responsivity was also obtained across several devices, and a box plot of the measured devices has been provided in the Supplementary Materials (fig. S5B). The device prepared by drop-casting PQDs on graphene showed a photoresponsivity of only 6×10^6 A W^{-1}. As the photocurrent generation in a single-layer graphene is very negligible due to ultrafast recombination and very low absorption (*23*), the major contribution to photogeneration arises from PQDs.

The figure of merit of the phototransistor, detectivity (D^*), was calculated on the basis of the equation

$$D^* = RA^{0.5}/(2qI_d)^{0.5} \quad (2)$$

where q is the absolute value of the electronic charge (1.6×10^{-19} C), A is the effective area of the device, and I_d is the dark current (*24*). D^* is the measure of the minimum optical power differentiated from the noise caused by shot noise from the dark current, which is the major contribution to the noise as compared with the other two noises, Johnson noise and thermal fluctuation "flicker" noise (*25*).

We determine a photodetectivity (D^*) of 4.72×10^{15} Jones and external quantum efficiency (EQE) (%) of 4.08×10^{10} for the G-PQD superstructure when illuminated with 430-nm light, as shown in Fig. 3B (inset). Our superstructure shows much enhanced sensitivity compared with other reported phototransistors, as shown in Table 1. In most semiconductor phototransistors, three transition modes occur: band-to-band, impurity-to-band, and quantum-well transitions (*26*). In our case, we favor band-to-band and impurity-to-band transitions because photon energy is absorbed by valence electrons of the PQDs when the energy of the incident photon is higher than the bandgap of PQDs. As a result, a photogenerated free charge carrier is generated. We find that because the PQDs were grown from graphene, the charge transfer from PQDs to graphene was very fast compared with a mixed or drop-casted/spin-coated sample. On the other hand, when the incident photons have less energy than the bandgap of PQDs, as band-to-band transition is not feasible, only electrons from the impurity levels can absorb the photons and get excited to the conduction band. This is followed by a transfer of electrons to graphene, leading to a very small photocurrent.

The schematic energy band diagram of the G-PQD superstructure is shown in Fig. 3 (C and D). The work function of a single-layer pristine graphene was around 4.56 ± 0.04 eV, whereas the Fermi level of PQD was 4 eV (*27*). We find that when PQDs are grown on the graphene sheet, the work function mismatch between the two materials leads to a built-in field developed at the interface of graphene and PQDs to align the Fermi levels. The Dirac point (V_{Dirac}), obtained from the drain-source resistance as a function of gate voltage under dark and illumination conditions, observes a drastic shift from above 80 to 70 V. We attribute this to the charge transfer from the PQDs to the graphene layer (fig. S6). Figure 3E shows the resistance as a function of back-gate voltage (V_{BG}) under different illumination intensities at a fixed drain-source voltage (V_{DS}) of 500 mV. As the light intensity increases, V_{Dirac}, at which the device resistance reaches its maximum value, shifts toward a higher voltage because of the photogating effect (*8*). Under illumination, the PQDs absorb the photon energy and generate electron-hole pairs, which are effectively dissociated at the graphene/PQD interface by the built-in field. We find that the photogenerated holes are transported to the graphene from PQDs, and the photogenerated electrons remain on the PQDs. The photogating effect, induced by the accumulated electrons in the PQDs, produces a hole current in the graphene through capacitive coupling (similar to the application of a negative voltage on graphene) and shifts V_{Dirac} of the G-PQD superstructure to a higher V_{BG}.

Furthermore, when $V_{BG} < V_{Dirac}$, the carrier transport in the graphene channel was hole dominant, which can increase the transfer rate of photogenerated holes, leading to a higher drain-to-source current. Therefore, a positive photoresponse was observed under illumination. In contrast, when $V_{BG} > V_{Dirac}$, the electron becomes the dominant charge carrier in the graphene channel, leading to a negative photoresponse or current quenching. This is due to the recombination of transferred photogenerated holes and induced electrons by the back-gate electrode. Moreover, as the illumination intensity increases, the trapped photogenerated electrons in PQDs

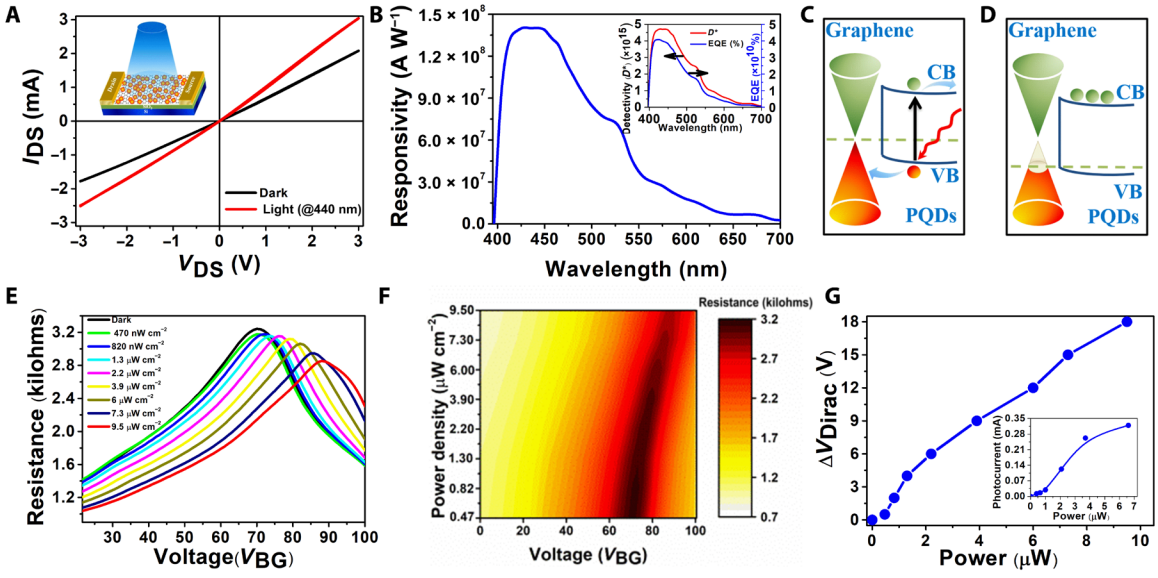

Fig. 3. G-PQD phototransistor. (**A**) Drain current (I_{DS}) versus drain voltage (V_{DS}) characteristic of the phototransistor under the dark and illumination intensity of 440 nm monochromatic light with zero gate voltage. Inset: Schematic of G-PQD superstructure phototransistor. (**B**) Spectral responsivity of G-PQD superstructure phototransistor. Inset: Detectivity and EQE of phototransistor under different wavelengths. Energy level diagram of the G-PQD superstructure under (**C**) photoexcitation and (**D**) photogating. VB and CB represent the valence band and conduction band of the PQDs. (**E**) Resistance as a function of back-gate voltage (V_{BG}) under different illumination intensities at a given drain-source voltage V_{DS} of 500 mV. (**F**) Two-dimensional plot of superstructure resistance as a function of optical power. (**G**) Shift of Dirac point as a function of incident light intensity. Inset: Variation of photocurrent under different illumination powers at 437 nm.

Table 1. Performance summary of previously reported graphene-QD–based phototransistor (MA: CH_3NH^{3+}, FA: $NH_2CH=CH^+$). MOF, metal-organic framework.

Active materials	R (A W^{-1})	D^* (Jones)	EQE (%)	λ (nm)	Thickness (nm)	Reference
$FAPbBr_3$-graphene	1.15×10^5		3.42×10^7	520		(*6*)
2D perovskite-graphene	1×10^5			532	125	(*7*)
$MAPbI_{3-x}Cl_x$-CNT	1×10^4	3.7×10^{14}			400	(*37*)
$MAPbBr_2I$-grapehene	6×10^5				250	(*38*)
PbS QD-graphene	2.6×10^4	5.5×10^{12}		637		(*39*)
MOF-graphene	1.25×10^6	6.9×10^{14}	5×10^8	325	140	(*40*)
$CsPbBr_3$-graphene nanoribbon	800	7.5×10^{14}	5×10^5	512	30	(*41*)
PbS QD-MoS_2	6×10^5	5×10^{11}		980	40–60	(*42*)
PbS QD-graphene	5×10^7	7×10^{13}		600	100	(*8*)
$MAPbBr_3$ film–graphene	180	1×10^9	5×10^4	400–800	>100	(*31*)
$MAPbBr_3$ PDs grown from graphene lattice	1.4×10^8	4.72×10^{15}	4.08×10^{10}	430–440	<20	This work

offer a more effective negative photogating effect by inducing more positive carriers in the graphene channel via capacitive coupling. This leads to the shift in the Dirac point toward a more positive back-gate voltage. The photoinduced shift of V_D at different intensities of monochromatic light (437 nm) is shown in Fig. 3F. Moreover, this photogating effect that occurs when light intensity increases results in more accumulation of induced charge in graphene channel, hence leading to an enhancement in surface potential (*28*, *29*). In this case, the photogating effect is controlled by light-induced gate voltage of the field-effect transistor (FET) structure and is very difficult to compare to the photogating effect observed in metal filament formation that can lead to pronounced resistive switching effects in QD-based photonic resistive random-access memory (*30*).

Figure 3G illustrates the shift of the Dirac point with incident power and the change of photocurrent ($I_{ph} = I_{light} - I_{dark}$) with respect to zero gate voltage at different light intensities. We observe that the

photocurrent increases as the incident photon power increases. As light intensity increases, more holes are generated and transferred to graphene, which induces a higher photogating effect and higher photocurrents. For bilayer films prepared by other deposition techniques on graphene for which there exists a thin space between the PQDs and the graphene films, the photocurrent response was much smaller than in the G-PQD device. To better understand the charge transfer effect, the photocurrent response was simulated using COMSOL. We compare two scenarios: (i) PQDs just touching the graphene surface forming a bilayer configuration and (ii) PQDs in close contact with the graphene film (i.e., considered as being inserted into the surface, grown from defect sites of graphene). The Fermi-Dirac semiconductor model was used to develop the G-PQD model, and continuous Fermi energy levels were used at the interface between the PQDs and the graphene films (*8*). To simplify the simulation, a 40 nm–by–40 nm area of the graphene film (film thickness, 0.3 nm) was used for all devices, and a total of 15 PQDs were attached randomly on the graphene film to form the G-PQD devices. The photocurrent effect was also simulated with two different PQD sizes (3 and 5 nm) in the G-PQD superstructure. A voltage of 1.5 μV was applied at the two ends of the film, and an incident plane wave with a wavelength of 430 nm was considered, as represented in Fig. 4 (A and B), respectively. We obtain a photocurrent response close to zero from simulations for graphene films, even at different light intensities. For G-PQD layers, the photocurrent is 0.3 pA under 150-nW illumination and 1.5-μV applied field. Among all devices, the photocurrent responses of G-PQD devices are the largest, which indicates that the charge transfer from the grown PQDs to the graphene film is much larger than that for PQDs deposited on the graphene film. This shows that growing PQDs on graphene provides a direct conduction path for charge transfer, which agrees with our experimental results.

Next, we investigated the transient response of the G-PQD superstructure. The transient photoresponse of the G-PQD superstructure under periodic white light illumination (33 mW cm^{-2}) with on and off time of 20 s was investigated, as shown in Fig. 4C. The results reveal a relatively fast and stable reproducible photoresponse. A quick rise of photocurrent as soon as the light is turned on was followed by a drop back to initial values when light was turned off. This indicates that the device can act as a light-activated switch. The response time for the photocurrent to rise up to 80% was about 0.45 s (Fig. 4D), which is comparable to the reported values in a graphene-perovskite structure (*31*). The photocurrent decay time was about 0.85 s for 50% decay from the maximum value. The longer response time was due to more complex factors, predominantly from the quantum capacitance of graphene and the time for relaxation charge transfer along ligands (*32*). Using this response time measurement, the photoconductive gain (*G*) (*8*) can be calculated on the basis of the equation

$$G = \tau_{\text{lifetime}}/\tau_{\text{transit}} = \tau_{\text{lifetime}}\mu V/l^2 \quad (3)$$

where τ_{lifetime} is the lifetime of the photogenerated carriers and τ_{transit} is the duration of the carrier transport within the channel. This was calculated using transistor mobility (μ) and applied drain-to-source voltage (*V*) of 0.5 V and a fixed channel length (*l*) of 15 μm. The calculated field-effect mobility of pristine single-layer graphene and the G-PQD superstructure are 2786 and 2580 $cm^2\ V^{-1}\ s^{-1}$, respectively. Therefore, the photoconductive gain of the G-PQD superstructure varies between 1.8×10^8 and 1×10^9 for lifetimes of 0.29 and 1.84 s, respectively. These values are very similar to the ones reported by Konstantatos *et al.* (*8*) in hybrid graphene-PbS QD phototransistor. The photoconductive gain can be further improved by increasing the carrier mobility of PQDs and introducing shorter chain ligands. We can attribute the high photoconductive gain and responsivity to the high charge carrier mobility of graphene as well as the direct charge transfer pathway between the PQDs and the graphene layers.

Neuromorphic photonic synapses and facial recognition

We observe a fast and stable photodetection property of the G-PQD superstructure when the gate voltage is maintained constant at 0 V. Tuning the gate voltage toward a positive direction can, however, limit the recombination of photogenerated carriers. Under light illumination, the gate-tunable device can therefore achieve a higher conductance state, which is retained even in the absence of light. This type of synaptic behavior, which is facilitated by gate tunability, is of great importance for neuromorphic computing.

In traditional von Neumann architecture, huge time and power spent in transporting data between memory and processor inevitably impose limitations in the performance and scalability of the structure, popularly known as the "von Neumann bottleneck" (*33*). This major drawback leads to severe problems in data centric applications, such as real-time image recognition, data classification, and natural language processing. Neuromorphic computing has emerged as a superior platform for parallel energy-efficient data processing with high accuracy and storage of information, which outperforms the von Neumann architecture (*33*). Figure 5A shows the anatomy of two biological neurons connected via a biological synapse. A synapse (Fig. 5B) acts as a channel of communication between two neurons. Information broadcasted from one neuron acting as presynaptic cell (transmitting neuron) is conveyed to the other acting as postsynaptic cell (receiving neuron) through a synapse. The synaptic behavior can be strengthened (potentiated) or weakened (depressed) using appropriate triggers of optical pulses. Measurements of synaptic plasticity, including short-term plasticity (STP), long-term plasticity (LTP), and long-term depression (LTD), are emulated to resemble the synaptic behavior of its biological counterpart. Here, we show that the G-PQD superstructure acts as an artificial photonic synapse, where the presynaptic signal is the external light stimuli in the form of optical pulses and the postsynaptic signal is the current obtained across the G-PQD channel keeping both drain source and gate voltage fixed (*29*).

To understand the synaptic dynamics of the device under different conditions of the presynaptic signal spikes, we recorded the change in conductance for light (specific wavelength of 440 nm) that has different intensities varying from 190 nW cm^{-2} to 1.1 μW cm^{-2} (Fig. 5C). Conductance of the device changes under the application of light when voltage biases were applied to the gate (10 V)/drain (0.5 V) electrodes of the device, while the source electrode was kept grounded. We achieve a higher level of conductance for light of highest intensity (1.1 μW cm^{-2}) as compared with the other intensities. At high intensity, we attribute enhancement in the conductance state to the formation of more photogenerated carriers. The effect of paired pulse facilitation (PPF), a special case of STP due to two closely spaced light pulses, is shown in Fig. 5D (see details in figs. S7 and S8). The PPF index increases when the photogenerated carriers from the first light spike, before recombination, are appended with those originating from the second light spike, resulting in an increase in the device conductance. The PPF ratio fades with the increasing

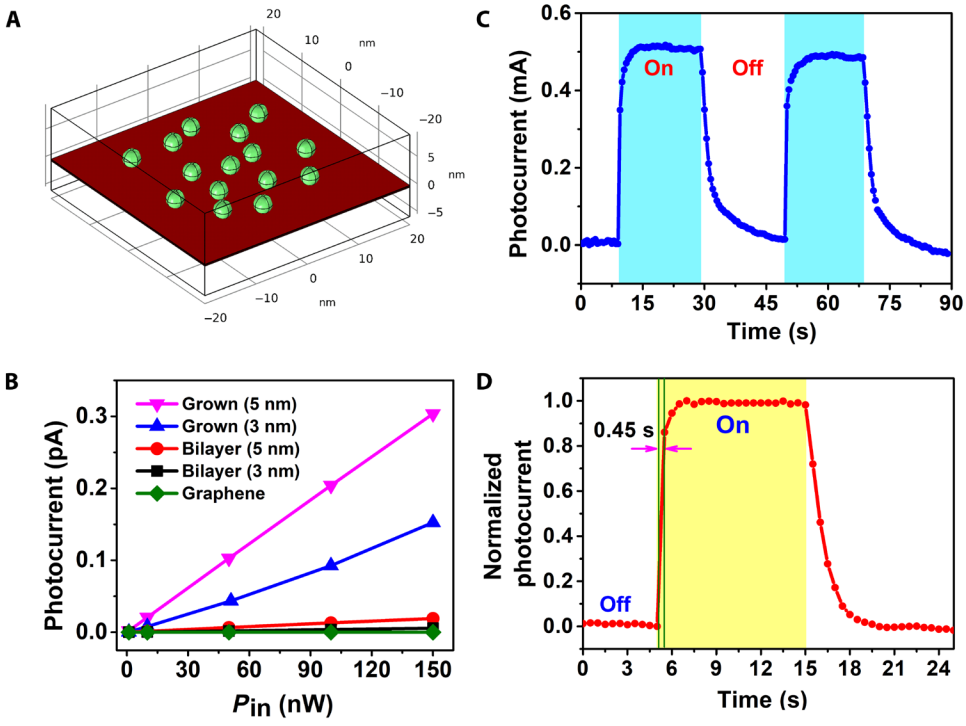

Fig. 4. COMSOL simulation and transient photoresponse. (**A**) Schematic of COMSOL simulation of PQDs of size 3 nm grown on a graphene film. (**B**) Simulated photocurrent versus input power. (**C**) Transient photoresponse under light illumination on and off conditions. (**D**) Normalized photocurrent response to on and off illumination.

photonic pulse intervals. A high value of PPF suggests the low rate of decay of the synaptic response, whereas a low value marks a high rate of decay. Therefore, it is seen that the index exponentially decreases with increasing off time between two pulses (delay between two pulses). This is indicative of the fact that reduction in off time between two pulses (≤10 s) amplifies the postsynaptic response, leading to STP. Therefore, when the device is triggered with repetitive training pulses, the learning effect in our device can be enhanced. In a training scheme where repetitive pulses (having off time of ~5 s) are used, the weight of the photonic synapse is governed by the number of pulses. Normalized conductance of the device for a varying number of pulses at a fixed wavelength of 440 nm with an intensity of 1.1 μW cm^{-2} is shown in Fig. 5E (see details in fig. S9). The normalized conductance attains a value of ~1.11 for one pulse and gradually increases as the number of pulses increases. The effect of (i) number of pulses and (ii) delay between the pulses on the device conductance is exponential in both cases, except for the number of pulses causing an exponential rise and the delay causing an exponential decay. It becomes essential to correlate the optimized off time between consecutive pulses (5 s in this case) along with the number of pulses (20 pulses in this case) to maximize conductance state. Figure 5F shows the variation in normalized conductance triggered by 20 presynaptic light spikes under a gate bias of 10 V. A change in conductance was obtained under application of light pulses and did not relax to its initial stage even when the light is switched off. LTP was induced in the device, which was sustained for 3000 s. LTP obtained by applying photonic pulses followed by LTD obtained by applying electrical pulses at drain is demonstrated in Fig. 5G. This shows the nonvolatile synaptic plasticity of our device. We find that negative pulses at drain help in depressing the potentiated device by detrapping the photogenerated carriers in the PQDs. The synaptic device shows paired pulse depression (PPD) of 99.03%, which is the percentage change in conductance of the second spike with respect to the first spike due to the application of the electrical pulses. PPD is observed when the first postsynaptic current (or postsynaptic conductance) is large, followed by a spike whose amplitude is less than the first and implies the inhibitory signal transmission. This contrasts with PPF, which is observed when the first postsynaptic current (or postsynaptic conductance) is small, and the second is larger than the first, which is based on excitatory signal transmission. We also observe gate-dependent LTP in Fig. 5H by increasing the gate bias. We find that both enhancement in conductance due to photogenerated carriers under illumination and capability of retention after removal of light increase as the gate becomes more positive. When gate voltage moves in the positive regime, electrons get trapped in the trap centers in graphene. These trapped charges lead to quasi p-doping of graphene. The higher the gate voltage, the larger the quasi p-doping of graphene. Under illumination, photogenerated holes are injected into the graphene from the PQDs, which contribute to the gain of photocurrent (or conductance) as holes are injected in a p-doped channel. This explains the jump in the conductance from the initial point to the final point, and this effect is emphasized when gate becomes more positive (holes being injected in the p^{++} channel). Moreover, the photogenerated holes injected into graphene cannot recombine with the electrons as the electrons are trapped even when the light is switched off because of positive gate voltage. The holes continue to flow in the system under the effect of drain voltage and maintain retention over a long time, resulting in LTP of the device. The energy consumption per synaptic event of optically stimulated synaptic devices is calculated using (*34*)

$$dE = S \times P \times dt \quad (4)$$

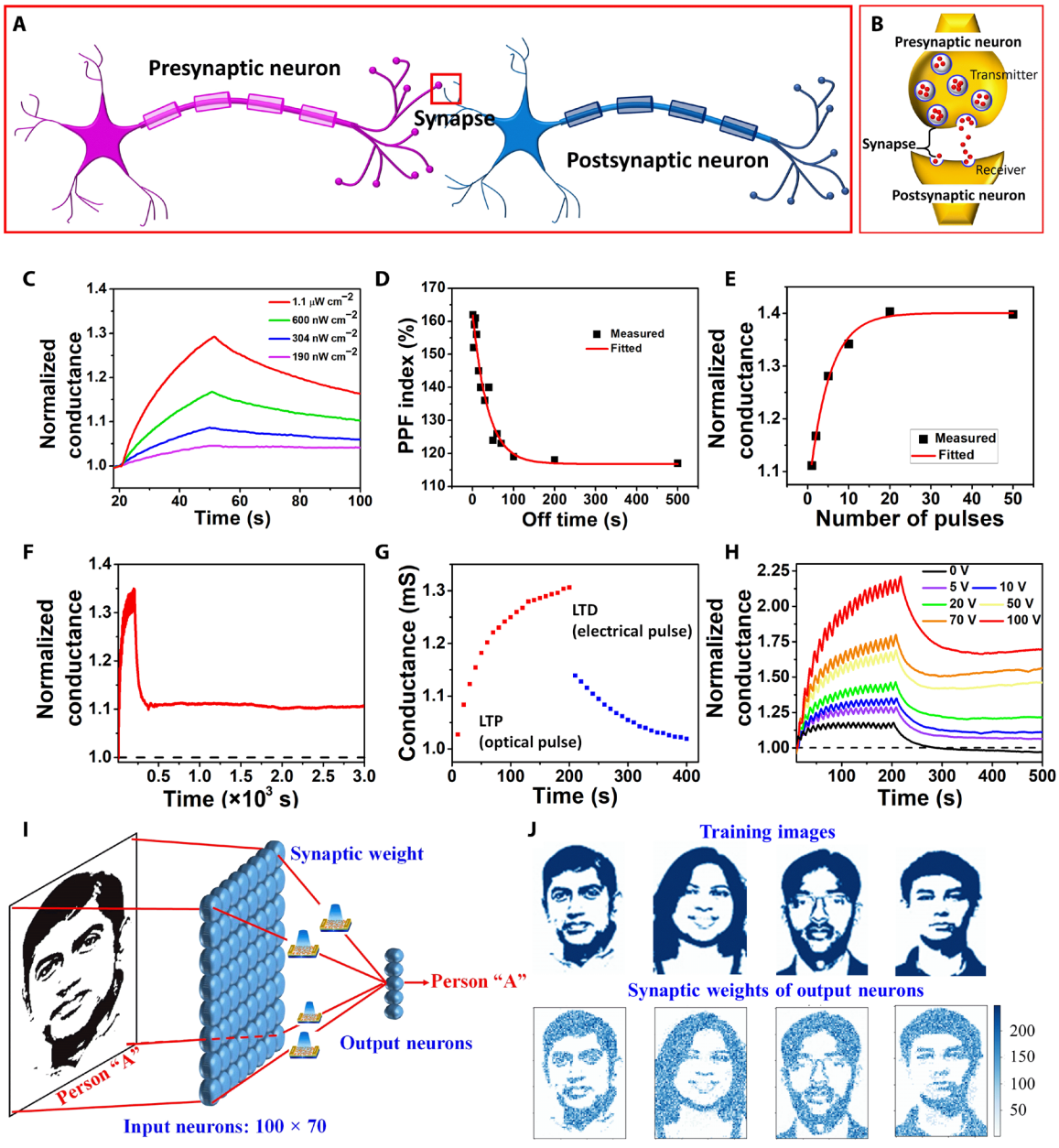

Fig. 5. Photonic synapse performance and facial recognition. (**A**) Anatomy of two interconnected human neurons via a synapse (red box). (**B**) Schematic representation of biological synapses. (**C**) Transient characteristic of the device (V_D = 0.5 V and V_G = 10 V) showing the change in conductance due to a single pulse of light of pulse width 30 s for varying light intensity. (**D**) PPF index of the device (V_D = 0.5 V and V_G = 10 V) due to varying off time between two consecutive light pulses having on time of 5 s. (**E**) Transient characteristic of the device (V_D = 0.5 V and V_G = 10 V) showing the change in conductance due to varying number of light pulses having on and off time of 5 and 5 s, respectively. (**F**) Retention of the long-term potentiated device (V_D = 0.5 V and V_G = 10 V) for 3×10^3 s after application of 20 optical pulses (on and off time of 5 and 5 s, respectively). (**G**) Nonvolatile synaptic plasticity of the device (V_G = 10 V) showing LTP by train of optical pulses (on and off time of 5 and 5 s, respectively) at V_D = 0.5 V and LTD by a train of electrical pulses (−0.5 V, on and off time of 1 and 1 s, respectively) at V_D. (**H**) Gate-dependent transient characteristic of the device (V_D = 0.5 V) after application of 20 optical pulses (on and off time of 5 and 5 s, respectively).(**I**), Neuron network structure for face recognition. Photo credit: Sreekanth Varma and Basudev Pradhan, UCF. (**J**) Real images (top) for training and the synaptic weights of certain corresponding output neurons (bottom). Photo credit (from left to right): Sreekanth Varma and Basudev Pradhan, UCF; Avra Kundu and Basudev Pradhan, UCF; Basudev Pradhan, UCF; and Basudev Pradhan, UCF.

where S is the area of the device and P is the power density of the input light at a spike duration of t. The calculation for our devices indicates that the energy consumption per synaptic event for potentiation is 36.75 pJ for the optimized spike duration of 5 s. We have also calculated energy consumption per synaptic event for devices showing photonic synaptic behavior reported in the literature and have compared them with the value obtained for our device (table S1). Our G-PQD synaptic device showed lower energy consumption with respect to the energy consumption calculated using the data of other similar devices given in the literature, as shown in table S1.

With the integrated optical information detection, processing, and retention capabilities of the G-PQD synaptic devices, they become a

potential candidate for human visual memory and in fields of pattern recognition. For real pattern recognition application, a dark current was chosen as a baseline. The fitted conductance curve of the device is shown in fig. S12, and the fitting parameters are shown in table S2. Those fitting parameters are important because they represent how a synaptic weight changes inside of the neuron network when training the network. For our optical synapses, both optical and electrical spikes were used to change the conductance. Using the fitted conductance properties of our device (*35*), we construct a spiking neural network to perform unsupervised machine learning and face recognition using Python. The simulation details are discussed in the Supplementary Materials. Portraits from four persons were used to train our neural network, and different portraits were used for testing. The network structure is shown in Fig. 5I. Each presynaptic neuron senses each pixel of the input images and transforms them into presynaptic spikes. After our synaptic devices, the postsynaptic signals were summed at the postsynaptic neuron, which could make it spike. Figure 5J displays the real images used for training and the synaptic weights of some corresponding output neurons, which shows the pattern recognition ability of this unsupervised spiking neural network with our device properties. By comparing the upper images (real images used for training) and the bottom images (synaptic weights of the corresponding output neurons), we find that our synapses catch the features from the portraits and realize facial recognition very well. In addition, to further detect the learning ability of our photonic synapses, 1000 figures from the MNIST (Modified National Institute of Standards and Technology) dataset were chosen for training, and 1000 different figures from the same dataset were chosen for testing, of which the results are shown in the Supplementary Materials. For real applications, if more output neurons are adapted and longer training time is used, higher recognition rates could be achieved.

DISCUSSION

In this study, we develop extremely thin superstructures by growing PQDs from graphene lattice by a defect-mediated crystal growth technique. We find that a highly enhanced charge transfer can be obtained because of the overlap of the π-electron clouds of PQDs and graphenes. The devices evaluated with the G-PQD superstructure exhibit high performances for phototransistor and photonic synapses. The phototransistors exhibit superior responsivity and specific detectivity to any other devices reported to date. The behavior is further validated by COMSOL simulations. Our approach can extend to other 2D materials, including transition metal dichalcogenides and other heterostructures, which opens the door to a new class of high-performing superstructure materials for many electronic and opto-electronic applications. The unique configuration of the PQD-graphene superstructure, which shows photonic synaptic behavior, is highly beneficial for facial recognition and future neuromorphic computing.

METHODS

Materials

Lead bromide ($PbBr_2$; 99.99%) and methylammonium bromide (CH_3NH_3Br; 99.5%), *N*,*N*-dimethylformamide (DMF; 99.9%), toluene (99.5%), butylamine, and oleic acid were purchased from Sigma-Aldrich and Ossila Ltd. All the chemicals were used without further purification.

Precursor preparation

Methylammonium lead bromide (CH_3NH_3PbBr) quantum dots (PQDs) were prepared by the LARP method (*5*). The precursor preparation involved solubilizing the precise ratio of $PbBr_2$ (0.2 mmol) and CH_3NH_3Br (0.16 mmol) salts in 5 ml of DMF. This was followed by the addition of 50 μl of butylamine and 500 μl of oleic acid to the perovskite precursor solution, which was ultrasonicated for 10 min.

Device fabrication

Bottom-gated FET structures were fabricated on a 300-nm-thick thermally grown SiO_2 dielectric on p^+ silicon. Single-layer graphene on copper foil purchased from Grolltex Inc. was wet transferred to an SiO_2 substrate as per the reported method (*36*). The graphene channel was patterned using photolithography and etched in oxygen plasma. Drain/source electrodes were patterned using photolithography, and 50-nm nickel was deposited using an electron beam evaporation process. The optical image of a representative graphene FET on an SiO_2/Si substrate is displayed in fig. S6. This fabricated graphene channel was dipped into a graphene precursor solution, and after 30 min, toluene was injected slowly into the solution, and PQDs were allowed to grow on the graphene channel for 1 hour. This was followed by thoroughly washing the sample to remove the excess precursor and PQDs and drying the samples by blowing N_2 gas.

Characterization

The topography of the PQD was characterized by TEM (FEI Tecnai F30 TEM) and a JEOL JEM 3010 instrument. The structures of the PQDs and G-PQDs were determined using XRD analysis (PANalytical Empyrean with 1.8-kW copper x-ray tube) and ultraviolet-visible (UV-vis) absorption spectroscopy (UV-vis spectrophotometer, Agilent Cary 300). The PL spectra of the films were recorded using fluorescence spectroscopy (fluorescence spectrometer, Horiba Nanolog FL3-11). The chemical bonding states of the materials were examined in detail by XPS (Physical Electronics 5400 Electron Spectroscopy for Chemical Analysis). The high-resolution XPS spectra corresponding to C-1s, N-1s, and I-3d doublets ($3d_{5/2}$ and $3d_{3/2}$) and Pb-4f doublets ($4f_{7/2}$ and $4f_{5/2}$) were analyzed using an XPS Peak version 4.1 program. Raman spectroscopy was performed on a WITec 300RA confocal Raman system with excitation laser at 532 nm and a 100× objective. Atomic force microscopy (AFM) measurements were carried out on a multimode system in contact mode. All phototransistor characteristics were measured in a probe station using a Keysight B1500A Semiconductor Device Analyzer under illumination from a halogen lamp fitted with a Newport monochromator. Light intensity was measured by a Newport power meter through calibrated Si photodiode. All photodetector measurements were conducted in ambient temperature.

Time-correlated single photon counting

TCSPC curves were collected while exciting the samples with a PicoQuant LDH-P-C-375 pulsed laser driven by a PDL 800-D controller. The repetition rate was set at 5 MHz. Laser intensity was adjusted to keep the photon emission rate below 5% of the laser repetition rate. Photons were collected on a single photon counting detector (PicoQuant, Micro Photon Devices, PDM series) connected to a PicoHarp 300 TCSPC module that detects the photon arrival time. The laser excitation was filtered with a 375-nm interference filter, while the emission was filtered by a 400-nm long pass emission

filter. TCSPC decay curves were fitted with FluoFit software (FluoFit Pro 2009, 4.4.0.1, PicoQuant). Because TCSPC decays were collected locally on G-PQD superstructures using a custom-built microscope, an instrument response function was not obtained, and decay curve fitting was accomplished via a tail fitting process.

Simulation

For COMSOL simulation (version 5.4), Semiconductor module, Wave Optics module, and Semiconductor-Electromagnetic Waves Coupling were used. Wave Optics were used to simulate the light absorption of the materials, in which a plane wave was incident on the film and the full field was calculated. Under light illumination, PQDs and graphene film domains were calculated by the Semiconductor module to get the photocurrent response, in which Fermi-Dirac carrier statistics were used.

SUPPLEMENTARY MATERIALS

Supplementary material for this article is available at http://advances.sciencemag.org/cgi/content/full/6/7/eaay5225/DC1

Supplementary Text
Section S1. Mobility calculation
Section S2. Pattern recognition
Fig. S1. PQD growth mechanism on single-layer graphene.
Fig. S2. XPS core level spectra of pristine PQDs.
Fig. S3. XPS core level spectra of G-PQDs.
Fig. S4. PQDs grown from graphene surface.
Fig. S5. Graphene FET.
Fig. S6. Shift of Dirac point due to PQDs grown on graphene.
Fig. S7. Transient photocurrent response.
Fig. S8. Calculation of PPF from the transient characteristic of the device for two consecutive light pulses.
Fig. S9. STP to LTP.
Fig. S10. Strategy to get testing dataset, which should be different from the images in the training dataset.
Fig. S11. Synaptic weights of each output neurons from the training of MNIST dataset.
Fig. S12. Fitted conductance change with pulse number of synapse.
Table S1. Comparison of our work with previously reported works in the literature in terms of energy consumption.
Table S2. Fitting parameters for potentiation and depression.
References (*43*–*48*)

REFERENCES AND NOTES

1. S. V. Morozov, K. S. Novoselov, M. I. Katsnelson, F. Schedin, D. C. Elias, J. A. Jaszczak, A. K. Geim, Giant intrinsic carrier mobilities in graphene and its bilayer. *Phys. Rev. Lett.* **100**, 016602 (2008).
2. B. Y. Zhang, T. Liu, B. Meng, X. Li, G. Liang, X. Hu, Q. J. Wang, Broadband high photoresponse from pure monolayer graphene photodetector. *Nat. Commun.* **4**, 1811 (2013).
3. F. Xia, T. Mueller, Y.-m. Lin, A. Valdes-Garcia, P. Avouris, Ultrafast graphene photodetector. *Nat. Nanotechnol.* **4**, 839–843 (2009).
4. R. R. Nair, P. Blake, A. N. Grigorenko, K. S. Novoselov, T. J. Booth, T. Stauber, N. M. Peres, A. K. Geim, Fine structure constant defines visual transparency of graphene. *Science* **320**, 1308 (2008).
5. F. Zhang, H. Zhong, C. Chen, X. G. Wu, X. Hu, H. Huang, J. Han, B. Zou, Y. Dong, Brightly luminescent and color-tunable colloidal $CH_3NH_3PbX_3$ (X = Br, I, Cl) quantum dots: Potential alternatives for display technology. *ACS Nano* **9**, 4533–4542 (2015).
6. R. Pan, H. Li, J. Wang, X. Jin, Q. Li, Z. Wu, J. Gou, Y. Jiang, Y. Song, High-responsivity photodetectors based on formamidinium lead halide perovskite quantum dot–graphene hybrid. *Part. Part. Syst. Char.* **35**, 1700304 (2018).
7. Y. Shao, Y. Liu, X. Chen, C. Chen, I. Sarpkaya, Z. Chen, Y. Fang, J. Kong, K. Watanabe, T. Taniguchi, A. Taylor, J. Huang, F. Xia, Stable graphene-two-dimensional multiphase perovskite heterostructure phototransistors with high gain. *Nano Lett.* **17**, 7330–7338 (2017).
8. G. Konstantatos, M. Badioli, L. Gaudreau, J. Osmond, M. Bernechea, F. P. G. de Arquer, F. Gatti, F. H. Koppens, Hybrid graphene–quantum dot phototransistors with ultrahigh gain. *Nat. Nanotechnol.* **7**, 363–368 (2012).
9. X. Hu, X. Zhang, L. Liang, J. Bao, S. Li, W. Yang, Y. Xie, High-performance flexible broadband photodetector based on organolead halide perovskite. *Adv. Funct. Mater.* **24**, 7373–7380 (2014).
10. T. C. Jellicoe, J. M. Richter, H. F. Glass, M. Tabachnyk, R. Brady, S. E. Dutton, A. Rao, R. H. Friend, D. Credgington, N. C. Greenham, M. L. Böhm, Synthesis and optical properties of lead-free cesium tin halide perovskite nanocrystals. *J. Am. Chem. Soc.* **138**, 2941–2944 (2016).
11. K. Tanaka, T. Takahashi, T. Ban, T. Kondo, K. Uchida, N. Miura, Comparative study on the excitons in lead-halide-based perovskite-type crystals $CH_3NH_3PbBr_3$ $CH_3NH_3PbI_3$. *Solid State Commun.* **127**, 619–623 (2003).
12. H. Mashiyama, Y. Kawamura, Y. Kubota, The anti-polar structure of $CH_3NH_3PbBr_3$. *J. Korean Phys. Soc.* **51**, 850–853 (2007).
13. D. Erdemir, A. Y. Lee, A. S. Myerson, Nucleation of crystals from solution: Classical and two-step models. *Acc. Chem. Res.* **42**, 621–629 (2009).
14. W. D. Callister, D. G. Rethwisch, *Materials Science And Engineering: An Introduction* (John Wiley & Sons New York, 2007), vol. 7.
15. M. R. Leyden, L. Meng, Y. Jiang, L. K. Ono, L. Qiu, E. J. Juarez-Perez, C. Qin, C. Adachi, Y. Qi, Methylammonium lead bromide perovskite light-emitting diodes by chemical vapor deposition. *J. Phys. Chem. Lett.* **8**, 3193–3198 (2017).
16. H. Ji, Z. Shi, X. Sun, Y. Li, S. Li, L. Lei, D. Wu, T. Xu, X. Li, G. Du, Vapor-assisted solution approach for high-quality perovskite $CH_3NH_3PbBr_3$ thin films for high-performance green light-emitting diode applications. *Acs Appl. Mater. Inter.* **9**, 42893–42904 (2017).
17. Y.-F. Xu, M.-Z. Yang, B.-X. Chen, X.-D. Wang, H.-Y. Chen, D.-B. Kuang, C.-Y. Su, A $CsPbBr_3$ perovskite quantum dot/graphene oxide composite for photocatalytic CO2 reduction. *J. Am. Chem. Soc.* **139**, 5660–5663 (2017).
18. H. C. Woo, J. W. Choi, J. Shin, S.-H. Chin, M. H. Ann, C.-L. Lee, Temperature-dependent photoluminescence of $CH_3NH_3PbBr_3$ perovskite quantum dots and bulk counterparts. *J. Phys. Chem. Lett.* **9**, 4066–4074 (2018).
19. J.-S. Chen, T. L. Doane, M. Li, H. Zang, M. M. Maye, M. Cotlet, 0D–2D and 1D–2D semiconductor hybrids composed of all inorganic perovskite nanocrystals and single-layer graphene with improved light harvesting. *Part. Part. Syst. Charac.* **35**, 1700310 (2018).
20. W. Geng, C.-J. Tong, Z.-K. Tang, C. Y. Yam, Y.-N. Zhang, W.-M. Lau, L.-M. Liu, Effect of surface composition on electronic properties of methylammonium lead iodide perovskite. *J. Materiomics* **1**, 213–220 (2015).
21. O. Cretu, A. V. Krasheninnikov, J. A. Rodríguez-Manzo, L. Sun, R. M. Nieminen, F. Banhart, Migration and localization of metal atoms on strained graphene. *Phys. Rev. Lett.* **105**, 196102 (2010).
22. X. Huang, T. R. Paudel, P. A. Dowben, S. Dong, E. Y. Tsymbal, Electronic structure and stability of the $CH_3NH_3PbBr_3$ (001) surface. *Phys. Rev. B* **94**, 195309 (2016).
23. P. A. George, J. Strait, J. Dawlaty, S. Shivaraman, M. Chandrashekhar, F. Rana, M. G. Spencer, Ultrafast optical-pump terahertz-probe spectroscopy of the carrier relaxation and recombination dynamics in epitaxial graphene. *Nano Lett.* **8**, 4248–4251 (2008).
24. Y. Tang, F. Wu, F. Chen, Y. Zhou, P. Wang, M. Long, W. Zhou, Z. Ning, J. He, F. Gong, Z. Zhu, S. Qin, W. Hu, A colloidal-quantum-dot infrared photodiode with high photoconductive gain. *Small* **14**, e1803158 (2018).
25. X. Gong, M. Tong, Y. Xia, W. Cai, J. S. Moon, Y. Cao, G. Yu, C.-L. Shieh, B. Nilsson, A. J. Heeger, High-detectivity polymer photodetectors with spectral response from 300 nm to 1450 nm. *Science* **325**, 1665–1667 (2009).
26. E. Rosencher, B. Vinter, *Optoelectronics* (Cambridge Univ. Press., Cambridge, England, 2002), pp. 300.
27. J. Endres, D. A. Egger, M. Kulbak, R. A. Kerner, L. Zhao, S. H. Silver, G. Hodes, B. P. Rand, D. Cahen, L. Kronik, A. Kahn, Valence and conduction band densities of states of metal halide perovskites: A combined experimental–theoretical study. *J. Phys. Chem. Lett.* **7**, 2722–2729 (2016).
28. Z. Lv, Y. Wang, Z. Chen, L. Sun, J. Wang, M. Chen, Z. Xu, Q. Liao, L. Zhou, X. Chen, J. Li, K. Zhou, Y. Zhou, Y. J. Zeng, S. T. Han, V. A. L. Roy, Phototunable biomemory based on light-mediated charge trap. *Adv. Sci.* **5**, 1800714 (2018).
29. Y. Wang, Z. Lv, J. Chen, Z. Wang, Y. Zhou, L. Zhou, X. Chen, S.-T. Han, Photonic synapses based on inorganic perovskite quantum dots for neuromorphic computing. *Adv. Mater.* **30**, 1802883 (2018).
30. Y. Wang, Z. Lv, Q. Liao, H. Shan, J. Chen, Y. Zhou, L. Zhou, X. Chen, V. A. L. Roy, Z. Wang, Z. Xu, Y.-J. Zeng, S.-T. Han, Synergies of electrochemical metallization and valance change in all-inorganic perovskite quantum dots for resistive switching. *Adv. Mater.* **30**, 1800327 (2018).
31. Y. Lee, J. Kwon, E. Hwang, C.-H. Ra, W. J. Yoo, J.-H. Ahn, J. H. Park, J. H. Cho, High-performance perovskite–graphene hybrid photodetector. *Adv. Mater.* **27**, 41–46 (2015).
32. X. Liu, N. Liu, M. Liu, Z. Tao, W. Kuang, X. Ji, J. Chen, W. Lei, Q. Dai, C. Li, X. Li, A. Nathan, Graphene nanomesh photodetector with effective charge tunnelling from quantum dots. *Nanoscale* **7**, 4242–4249 (2015).
33. H. Tsai, S. Ambrogio, P. Narayanan, R. M. Shelby, G. W. Burr, Recent progress in analog memory-based accelerators for deep learning. *J. Phys. D Appl. Phys.* **51**, 283001 (2018).
34. Z. Ni, *et al.* in *2018 IEEE International Electron Devices Meeting (IEDM)* (IEEE), pp. 38.35. 31–38.35. 34.

35. S. Kim, B. Choi, M. Lim, J. Yoon, J. Lee, H.-D. Kim, S.-J. Choi, Pattern recognition using carbon nanotube synaptic transistors with an adjustable weight update protocol. *ACS Nano* **11**, 2814–2822 (2017).
36. J. Chan, A. Venugopal, A. Pirkle, S. McDonnell, D. Hinojos, C. W. Magnuson, R. S. Ruoff, L. Colombo, R. M. Wallace, E. M. Vogel, Reducing extrinsic performance-limiting factors in graphene grown by chemical vapor deposition. *ACS Nano* **6**, 3224–3229 (2012).
37. F. Li, H. Wang, D. Kufer, L. Liang, W. Yu, E. Alarousu, C. Ma, Y. Li, Z. Liu, C. Liu, N. Wei, F. Wang, L. Chen, O. F. Mohammed, A. Fratalocchi, X. Liu, G. Konstantatos, T. Wu, Ultrahigh carrier mobility achieved in photoresponsive hybrid perovskite films via coupling with single–walled carbon nanotubes. *Adv. Mater.* **29**, 1602432 (2017).
38. Y. Wang, Y. Zhang, Y. Lu, W. Xu, H. Mu, C. Chen, H. Qiao, J. Song, S. Li, B. Sun, Y.-B. Cheng, Q. Bao, Hybrid graphene–perovskite phototransistors with ultrahigh responsivity and gain. *Adv. Opt. Mater.* **3**, 1389–1396 (2015).
39. L. Zheng, W. Zhou, Z. Ning, G. Wang, X. Cheng, W. Hu, W. Zhou, Z. Liu, S. Yang, K. Xu, M. Luo, Y. Yu, Ambipolar graphene–quantum dot phototransistors with CMOS compatibility. *Adv. Opt. Mater.* **6**, 1800985 (2018).
40. K. P. Bera, G. Haider, M. Usman, P. K. Roy, L.-I. Lin, Y.-M. Liao, C. R. P. Inbaraj, Y.-R. Liou, M. Kataria, K.-L. Lu, Y.-F. Chen, Trapped photons induced ultrahigh external quantum efficiency and photoresponsivity in hybrid graphene/metal–organic framework broadband wearable photodetectors. *Adv. Funct. Mater.* **28**, 1804802 (2018).
41. X. Liu, W. Kuang, H. Ni, Z. Tao, Q. Huang, J. Chen, Q. Liu, J. Chang, W. Lei, A highly sensitive and fast graphene nanoribbon/$CsPbBr_3$ quantum dot phototransistor with enhanced vertical metal oxide heterostructures. *Nanoscale* **10**, 10182–10189 (2018).
42. D. Kufer, I. Nikitskiy, T. Lasanta, G. Navickaite, F. H. Koppens, G. Konstantatos, Hybrid 2D–0D MoS_2–PbS quantum dot photodetectors. *Adv. Mater.* **27**, 176–180 (2015).
43. H. Zhong, Z. Zhang, H. Xu, C. Qiu, L.-M. Peng, Comparison of mobility extraction methods based on field-effect measurements for graphene. *AIP Adv.* **5**, 057136 (2015).
44. H. Tian, X. Wang, F. Wu, Y. Yang, T.-L. Ren, in *2018 IEEE International Electron Devices Meeting (IEDM)* (IEEE), pp. 38.36. 31–38.36. 34.
45. S. Qin, F. Wang, Y. Liu, Q. Wan, X. Wang, Y. Xu, Y. Shi, X. Wang, R. Zhang, A light-stimulated synaptic device based on graphene hybrid phototransistor. *2D Mater.* **4**, 035022 (2017).
46. S. Dai, X. Wu, D. Liu, Y. Chu, K. Wang, B. Yang, J. Huang, Light-stimulated synaptic devices utilizing interfacial effect of organic field-effect transistors. *ACS Appl. Mater. Interfaces* **10**, 21472–21480 (2018).
47. H. K. Li, T. P. Chen, P. Liu, S. G. Hu, Y. Liu, Q. Zhang, P. S. Lee, A light-stimulated synaptic transistor with synaptic plasticity and memory functions based on $InGaZnO_x$–Al_2O_3 thin film structure. *J. Appl. Phys.* **119**, 244505 (2016).
48. M. Lee, W. Lee, S. Choi, J. W. Jo, J. Kim, S. K. Park, Y. H. Kim, Brain-inspired photonic neuromorphic devices using photodynamic amorphous oxide semiconductors and their persistent photoconductivity. *Adv. Mater.* **29**, 1700951 (2017).

Acknowledgments: We would like to thank D. Fox for drawing fig. S4. **Funding:** J.T. acknowledges the NSF (CAREER: ECCS-1351757) for the financial support. E.B. acknowledges the NASA Space Technology Research Fellowship Program for the XPS analysis. B.P. thanks the Indo-U.S. Science and Technology Forum (IUSSTF), DST, government of India for providing fellowship under the BASE program (ref. BASE2018 Fellowship/1/BP) in the United States. J.C. thanks the P3 Pre-Eminent Post-Doctoral Research Fellowship. T.R. acknowledges support from the NSF (CAREER: ECCS-1845331). **Author contributions:** B.P. and F.C. prepared the PQD materials. F.C. contributed to the TEM measurements. S.D., D.D., and A.K. fabricated the graphene FETs. T.R. and S.D. conceived the photonic synapse experiments. B.P. and S.D. designed, fabricated, and conducted the phototransistor and photonic synapse measurements. J.C. and E.B. carried out the structural characterization of the samples, and D.P. investigated the charge transport mechanism. J.L. did the COMSOL simulation and pattern recognition. L.T. carried out the AFM and Raman characterization. A.T. and A.G. performed the PL lifetime measurements. All the authors contributed to the discussion of the paper and approved the manuscript. J.T. conceived the idea and directed the scientific research of this work. **Competing interests:** The authors declare that they have no competing interests. **Data and materials availability:** All data needed to evaluate the conclusions in the paper are present in the paper and/or the Supplementary Materials. Additional data related to this paper may be requested from the authors.

Submitted 26 June 2019
Accepted 25 November 2019
Published 12 February 2020
10.1126/sciadv.aay5225

Citation: B. Pradhan, S. Das, J. Li, F. Chowdhury, J. Cherusseri, D. Pandey, D. Dev, A. Krishnaprasad, E. Barrios, A. Towers, A. Gesquiere, L. Tetard, T. Roy, J. Thomas, Ultrasensitive and ultrathin phototransistors and photonic synapses using perovskite quantum dots grown from graphene lattice. *Sci. Adv.* **6**, eaay5225 (2020).